

Original Research Article

Analytical stiffness prediction method for idealized passive dynamic ankle-foot orthoses under standardized bench test conditions

O. Strenge^{1*} and D. Hochmann¹

¹ Biomechanics Research Laboratory, FH Münster University of Applied Sciences, Steinfurt, Germany

* Corresponding author, email: ole.strenge@fh-muenster.de

Received March 15, 2026; Accepted April 19, 2026; Published online June 14, 2026

© 2026 Ole Strenge; licensee Infinite Science Publishing

This is an Open Access abstract distributed under the terms of the Creative Commons Attribution License, which permits unrestricted use, distribution, and reproduction in any medium, provided the original work is properly cited (<http://creativecommons.org/licenses/by/4.0>).

Abstract: Passive dynamic ankle-foot orthoses (PD-AFOs) are used to stabilize the foot and reduce muscle load in patients with neuromuscular impairments. A PD-AFO is characterized by its stiffness - the relationship between its resistive torque and its deflection angle. AFO stiffness plays a decisive role in the quality of patient care. To date, only a few approaches for predicting the stiffness of non-experimental and non-articulated PD-AFOs prior to manufacturing can be found in the literature. All these approaches use finite element analysis. Therefore, the objective of this work was to develop and evaluate a simplified analytical method for predicting the stiffness of idealized PD-AFOs on a standardized test bench prior to manufacture, providing an alternative to finite element analysis. This is particularly relevant in the context of additive manufacturing, where geometry can be freely adapted. The proposed calculation method is based on Castigliano's energy theorem and was demonstrated for PD-AFO designs featuring posterior leaf springs or posterior struts made from plastic (3D-printed) or carbon composite. The calculations can be performed with pen and paper. Validation was performed by comparing calculated stiffness values with measurements on a test bench. On average, the method yields deviations of less than 5% between the calculated and measured stiffness values for PD-AFOs with posterior leaf springs. However, due to deformations of the test bench, the calculated results for PD-AFOs with posterior struts deviate significantly from the measured results. This can be accounted for by a simple adjustment and calibration of the model. For the calibrated model, the calculated values deviate by less than 15% on average from the measured values. This simplified analytical approach offers a practical tool for designers to estimate PD-AFO stiffness during the development phase, enabling stiffness prediction prior to manufacture and thereby supporting patient-specific design decisions.

I. Introduction

Passive dynamic ankle-foot orthoses (PD-AFOs) stabilize the foot and reduce muscle load in patients with neuromuscular impairments [1–3]. They work by applying a resistive torque to the lower extremities, mainly in the sagittal plane [4–6], generated by a functional dynamic element such as a posterior leaf spring (see, e.g., Wach et al. [7] or Bartonek et al. [8]) or a posterior strut (see, e.g., Tavernese et al. [9] or Hoyt et al. [10]). These functional elements are typically made from plastic or carbon composite. Manufacturing methods include customized craftsmanship, industrial production, and increasingly, additive manufacturing (3D-printing) [11–15]. In literature, the behavior of a PD-AFO is characterized by its stiffness k_{AFO} . k_{AFO} describes the relationship between the

resistive torque $T_{AFO}(\varphi)$ of the orthosis and its angular deflection φ . Although some AFOs exhibit a non-linear stiffness behavior, a linear relationship between $T_{AFO}(\varphi)$ and φ is usually assumed, with k_{AFO} reflecting the constant proportionality factor [5,6]. Therefore, the following applies:

$$T_{AFO}(\varphi) = k_{AFO} \cdot \varphi \quad (1)$$

Various studies show that the stiffness of a PD-AFO significantly influences the quality of patient care [16,17].

To determine AFO stiffness, bench testing is by far the most established and validated method for measuring AFO stiffness [5,6]. The drawback of bench testing is that it can only be performed post-manufacture [5,6]. This is why it

cannot inform design decisions prior to fabrication. In clinical practice, however, the ability to predict stiffness from geometric and material parameters before manufacturing would be highly valuable: it would allow clinicians and designers to select or adapt orthosis geometry to meet a patient-specific stiffness target. This is particularly relevant in the context of additive manufacturing, where geometry can be freely adapted [18–20].

To address this, literature reports the use of Finite element analysis (FEA) to predict AFO stiffness prior to manufacture. However, this process is often limited to specific designs and requires complex simulations, hindering generalization and integration into manual manufacturing processes [20–27].

An analytical method that enables stiffness prediction without requiring FEA software or test bench access would therefore complement existing measurement approaches and support both design optimization and clinical prescription.

To the best of the authors' knowledge, no closed-form analytical solution for predicting stiffness of non-experimental and non-articulated PD-AFOs prior to manufacture has been reported in the literature. For this reason, this study focuses on the development and evaluation of a simplified analytical calculation method that can be used to estimate the stiffness of standardized PD-AFO on a test bench. To demonstrate and validate the method, it was applied to PD-AFOs with 3D-printed functional elements but was also tested with functional elements used in everyday clinical practice. The calculation can be performed using Castigliano's energy methods and thus with pen and paper, without complex FEA. The validation of the method is limited to orthosis types with L-shaped posterior leaf springs, such as the Carbon Ankle Seven (CA7, Ottobock, Duderstadt, Germany) or similar designs [7,8,28–30], or with posterior struts [9,10,31–35].

It should be noted that the presented equations are only applicable for stiffness measurements on test benches similar to the one described in this work, as the predicted stiffnesses are inextricably linked to the specific experimental setup and inherent stiffness of the test bench itself. Nevertheless, the methodology can also be applied to other test benches, as long as the assumptions made are adjusted accordingly.

II. Material and methods

The following section describes the general methodology of the study, the calculation procedure, and all materials required for the evaluation.

II.I. Study design

The calculation procedure below was developed to predict the stiffness of standardized PD-AFOs on a test bench, by

idealizing the system of orthosis and test bench. To evaluate it, idealized PD-AFO's functional elements were 3D-printed from five different materials. To test whether the method is applicable to other materials, a posterior leaf spring and a posterior strut used in clinical practice were also tested. Material properties were determined via three-point bending tests. Using specially manufactured test mounts, the idealized system's properties were physically reproduced, and the system's stiffness was measured on the test bench. Simultaneously, the system's stiffness was predicted with the calculation method and measured and calculated results were compared.

II.II. Orthosis types

Orthosis types featuring an L-shaped posterior leaf spring or a posterior strut were selected to demonstrate the calculation procedure. These functional elements have an approximately constant cross-sectional area, and the geometry of the elements can be easily approximated using parameterizable basic geometric shapes.

II.III. Test bench

All stiffness measurements of the idealized orthoses were performed on a custom-built test bench similar to the one presented by Cappa et al. [36]. The setup is and shown in Fig. 1.

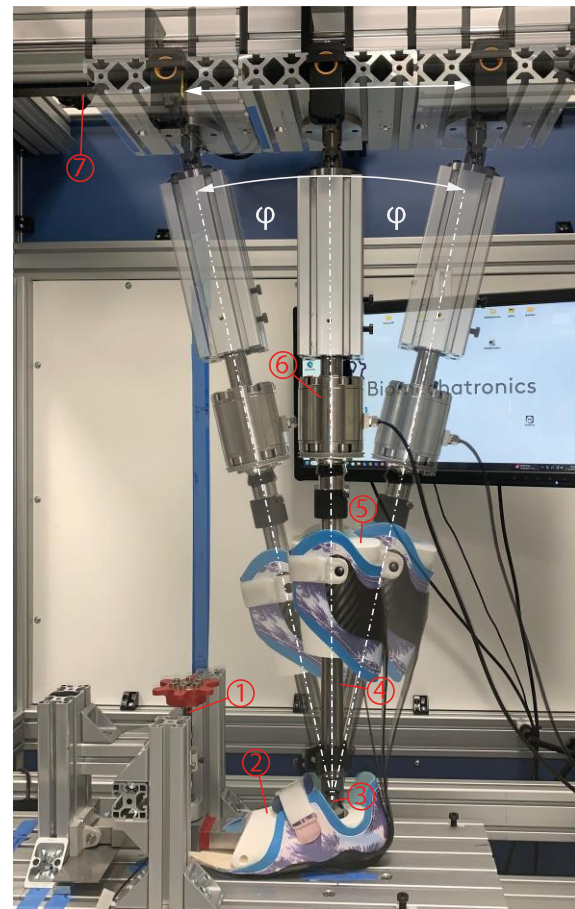


Figure 1: Orthosis on test bench, 1 = trapezoidal spindle, 2 = foot model, 3 = universal joint at VAJC height, 4 = linear guide, 5 = linear guided leg model, 6 = 6-component force transducer, 7 = belt drive.

Here, a translational movement induced by a belt drive (Motor: AZM69AC, Oriental Motor Co., Tokyo, Japan; belt system: Timing-belt drive, item Industrietechnik GmbH, Solingen, Germany) is converted into a rotation around a patient-specific virtual ankle joint center (VAJC). The orthosis foot cuff is clamped to a base plate using a 3D-printed model of the patient's foot which is pressed down via a trapezoidal spindle (RPTS-10x2, Dold Mechatronik, Haslach, Germany). The orthosis calf cuff is attached to a linearly guided, also 3D-printed lower leg model. The linear guide (SSP30, Dr. Tretter Maschinenelemente, Rechberghausen, Germany) is connected to the foot model at the height of the VAJC via a universal joint. The belt drive allows the linear guide and thus also the lower leg model to be deflected in the sagittal plane, while an intermediate 6-component force transducer (K6D68 1kN/20Nm/CG, ME-Meßsysteme, Hennigsdorf, Germany) measures the internal forces in the linear guide. The test bench's deflection angle φ is calculated from the belt travel and the geometric relationships. Finally, the orthosis stiffness can be determined as a linear regression of the angle-to-torque curve from the measured forces, the geometric relationships, and the deflection angle.

II.IV. Calculation method

The derivation of the mathematical model of a PD-AFO on the described test bench follows the steps outlined below, which are presented here in a highly condensed form but are described in greater detail in the Appendix:

1. Mechanical abstraction and modeling
2. Definition of assumptions
3. Establishing deformation equations using Castigliano's energy theorem
4. Determination of the sought-after unknowns
5. Calculation of AFO stiffness

Mechanical abstraction and modeling:

In order to mathematically model an orthosis on the test bench, the system must first be idealized. The following calculations are based on the laws of elastostatics and Castigliano's second theorem, neglecting shear stresses (Euler-Bernoulli beam theory) and assuming small deformation angles.

For idealization, several assumptions must first be made in order to eliminate influence factors that are difficult to model, such as the deformation of the cuffs, the stretching of the straps, or the friction of the linear guide. Furthermore, geometric relationships such as the curvature of the functional element must be approximated using geometrically parameterizable shapes. In addition, the contour of the cross-section along the functional element must be mathematically parameterized. Since a variable cross-sectional area significantly complicates the calculations, only functional elements with an approximately constant cross-section were selected for this

study, resulting in the PD-AFO types aforementioned. However, the method can also be applied to other types of PD-AFOs, provided the same assumptions can be made.

In summary, this results in the following assumptions, which were used to model the orthosis-test-bench-system:

- A1. All functional elements have a constant cross-section
- A2. The cuffs and test bench components are ideally rigid
- A3. All components are massless
- A4. The test bench's linear guide is frictionless

Using assumptions A1-A4, the real orthosis-test-bench-system can be converted into an idealized orthosis model (see Fig. 2b). The idealized model consists of an ideally rigid foot cuff into which the functional element is clamped. The calf cuff is also ideally rigid and mounted frictionlessly on the linear guide. The functional element is ideally clamped into the calf cuff. The geometry of a posterior leaf spring was approximated using a straight bending beam with a final 90° bend. Similarly, the posterior struts were modelled as straight bending beams.

The idealized orthosis model was then abstracted into a mechanical equivalent model (see Fig. 2c).

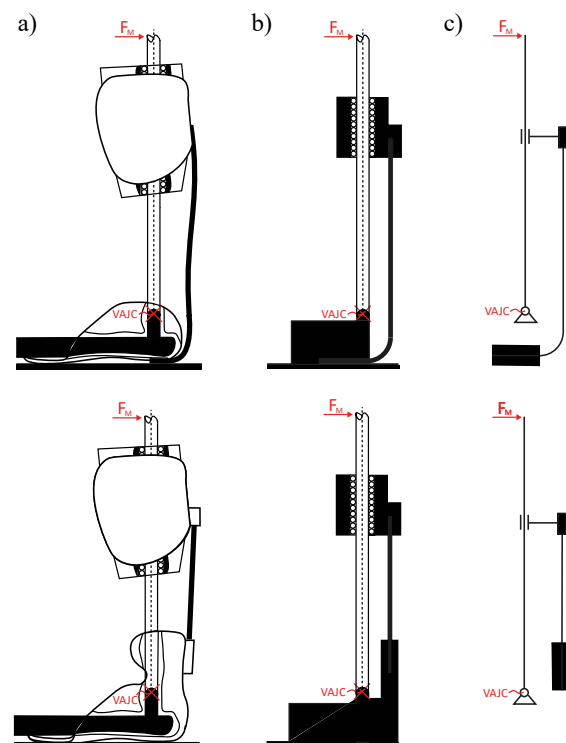


Figure 2: Idealization and modeling of an PD-AFO on the test bench, a) Real PD-AFO on the test bench, b) Idealized orthosis with rigid cuffs and idealized shape of the functional element, c) Mechanical equivalent model of the idealized orthosis used for derivation of the analytical model.

All further considerations are carried out using the example of an orthosis with a posterior leaf spring, but the calculation steps for an orthosis with posterior struts are analogous.

On the test bench, the resistive torque T_{AFO} relative to the VAJC is obtained by (see Fig. 3a):

$$T_{AFO}(\varphi) = F_M(\varphi) \cdot l_M \quad (2)$$

Together with equation (1) and the geometric relationships of the mechanical equivalent model, the calculated stiffness relative to the VAJC is:

$$k_{AFO} = \frac{F_M(\varphi) \cdot l_M}{\varphi} \quad (3)$$

Where φ is the deflection of the test bench.

The following relationship can be derived from the geometric conditions and the system's free body diagram (Fig. 3c):

$$k_{AFO} = \frac{T_{LS}(\varphi) + F_{LS}(\varphi) \cdot l_{FAP}}{\varphi} \quad (4)$$

Here, $T_{LS}(\varphi)$ and $F_{LS}(\varphi)$ are the torques/forces transferred from the functional element to the test bench, l_{FAP} is the distance between the VAJC and the point of force application (approx. at the center of the calf cuff).

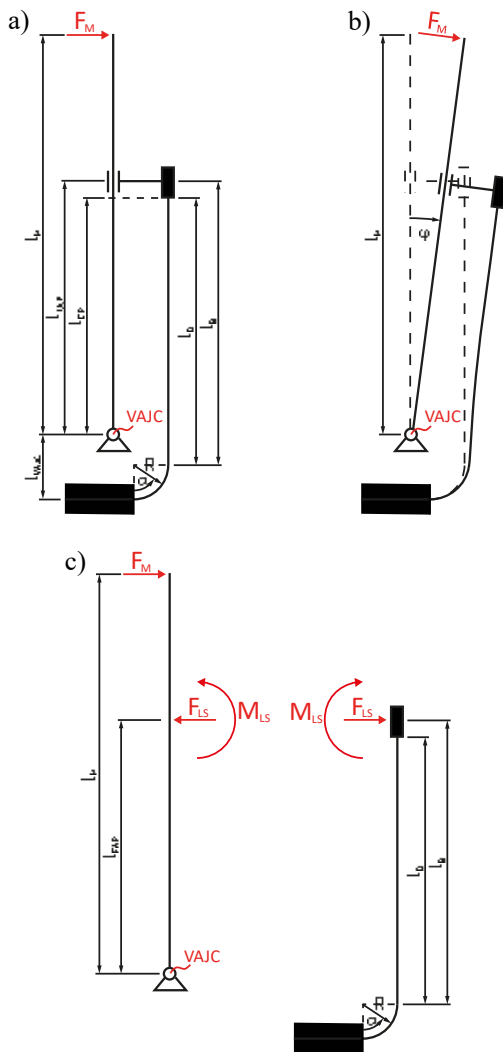


Figure 3: Properties of the mechanical equivalent model, a) Geometric relationships, b) Deflection of the idealized orthosis, c) Free body diagram of test bench and functional element.

Definition of assumptions:

To calculate $T_{LS}(\varphi)$ and $F_{LS}(\varphi)$, the relationship of the functional element's deformation state (defined by its deflection f and deformation angle ω) and the test bench's deflection angle φ must be found. With the help of two further assumptions, the relationship between f and ω with φ can be established, thus $T_{LS}(\varphi)$ and $F_{LS}(\varphi)$ can be determined and finally the equation for stiffness prediction can be found.

These assumptions are as follows:

A5. The functional element's deformation angle ω at the point of its attachment to the calf cuff (at height $l_D + R$) equals the deflection angle of the test bench φ (see also Fig. 4a):

$$\varphi = \omega \quad (5)$$

A6. The functional element's deflection f at the point of its attachment to the calf cuff (at height $l_D + R$) equals the horizontal distance traveled by the test bench this height. Under the small angle approximation follows (see also Fig. 4b):

$$\varphi \cdot l_{EP} = f \quad (6)$$

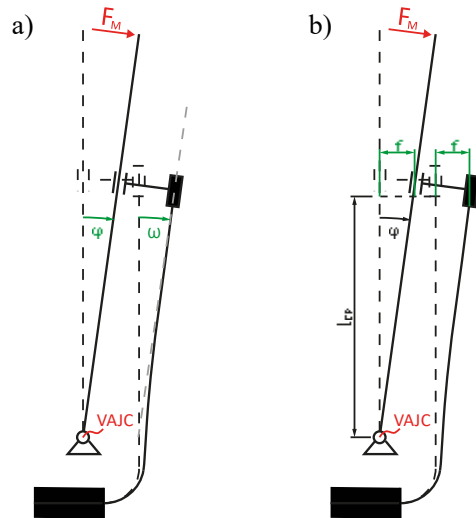


Figure 4: Visualization of assumptions, a) Assumption A5 (the functional element's deformation angle ω equals the test bench's deflection angle φ), b) Assumption A6 (the functional element's deflection f equals the horizontal distance traveled by the test bench at same height).

Establishing deformation equations using Castigliano's energy theorem:

With assumptions A5 and A6 the required relationship between the deformation state of the functional element and the test bench's deflection angle is found. Using this relationship and Castigliano's energy theorem, the forces/torques transmitted from the functional element to the test bench can be expressed as a function of φ . To do this, Castigliano's deformation equations must first be formulated, with $T_{LS}(\varphi)$ and $F_{LS}(\varphi)$ implicitly included in them. The deformation equations for a loading condition such as the one given here are as follows:

$$\Theta = \sum_i \left(\int \frac{M_{C,i} \delta M_{C,i}}{E \cdot I \delta T_j} dx \right) \quad (7)$$

$$f = \sum_i \left(\int \frac{M_{C,i} \delta M_{C,i}}{E \cdot I \delta F_j} dx \right) \quad (8)$$

Here, $M_{C,i}$ represents the internal bending moment in the individual sections i . T_j and F_j denote the externally acting torques and forces at the point of evaluation of Θ and f . E is the flexural modulus, and I is the area moment of inertia of the structural element.

To solve equations (7) and (8) several integrals must be solved, which depend on the distribution of the externally acting torques and forces, the geometric relationships of the system, and the area moment of inertia and modulus of elasticity of the structural element. Since only point loads act in the given scenario and the flexural modulus as well as the area moment of inertia remain constant, the integrals depend exclusively on the geometric relationships of the system. Solving the integrals and substituting the results into the equations (7) and (8) yields the following deformation equations (for the sake of better readability, the geometric relationships derived from the integrals have been summarized in the coefficients A-D):

$$\Theta = \frac{1}{E \cdot I} (F_{LS}(\varphi) \cdot A + T_{LS}(\varphi) \cdot B) \quad (9)$$

$$f = \frac{1}{E \cdot I} (F_{LS}(\varphi) \cdot C + T_{LS}(\varphi) \cdot D) \quad (10)$$

The coefficients A-D depend solely on the geometry of the idealized system (see Figure 3a). For the two idealized orthosis types examined in this study the coefficients can be found in Table 1. A more detailed description of how to solve the integrals and derive the coefficients for the given system can be found in the Appendix chapters A.II.-A.IV.

Table 1: Coefficients of calculation.

A	$R^2 + \frac{\pi}{2} R \cdot l_B + l_B \cdot l_D - \frac{1}{2} l_D^2$
B	$\frac{\pi}{2} R + l_D$
C	$\frac{\pi}{4} R^3 + (l_B + l_D) \cdot R^2 + \frac{\pi}{2} \cdot R \cdot l_B \cdot l_D + \frac{1}{2} \cdot l_B \cdot l_D^2 - \frac{1}{6} \cdot l_D^3$
D	$R^2 + \frac{\pi}{2} R \cdot l_D + \frac{1}{2} \cdot l_D^2$

Determination of the sought-after unknowns:

Substituting equations (9) and (10) into (5) and (6) yields a linear system of equations that solely depends on the flexural modulus E , the area moment of inertia I and the geometric relationships of the idealized orthosis. Solving

this linear system of equations for $T_{LS}(\varphi)$ and $F_{LS}(\varphi)$ yields the explicit relationship of the acting torques/forces and φ :

$$T_{LS}(\varphi) = E \cdot I \cdot \varphi \cdot \frac{l_{EP} \cdot A - C}{D \cdot A - B \cdot C} \quad (11)$$

$$F_{LS}(\varphi) = E \cdot I \cdot \varphi \cdot \frac{l_{EP} \cdot B - D}{C \cdot B - A \cdot D} \quad (12)$$

Calculation of AFO stiffness:

Substituting these equations into equation (4) yields the final equation for stiffness prediction of the idealized orthosis:

$$k_{AFO} = E \cdot I \cdot \left(\frac{l_{EP} \cdot A - C}{D \cdot A - B \cdot C} + l_{FAP} \cdot \frac{l_{EP} \cdot B - D}{C \cdot B - A \cdot D} \right) \quad (13)$$

Using this equation, the stiffness of an idealized orthosis of aforementioned AFO types can now be calculated. To do this, only the flexural modulus E , the area moment of inertia I , and the geometric values l_{FAP} , l_{EP} , l_B , l_D , and R need to be determined. For AFOs of other shapes, the calculation procedure can be applied analogously; in this case, only the coefficients need to be redefined according to the described procedure.

II.V. Test setup

To evaluate the calculation method, functional elements for both idealized orthosis types were 3D-printed from different materials. To achieve a wide range of stiffness values, materials with a high variation in their stiffness properties were selected. The following materials were chosen based on their technical data sheets (TDS): ecoPLA (niceshops GmbH, Paldau, Austria), niceBIO (niceshops GmbH, Paldau, Austria), Green-TEC Pro (FD3D GmbH, Lustenau, Austria), and PPACF (Bambu Lab, Shenzhen, China) using a V-Core 4 500 mm IDEX FDM printer (RatRig, Faro, Portugal). Three specimens per variant and seven ISO 178:2019-compliant three-point bending specimens were printed per material in the same batch [37]. Additionally, two specimens made of Markforged Onyx (Markforged, Waltham, USA) with continuous carbon fiber reinforcement (CCFR) were printed on a X7 FDM printer (Markforged, Waltham, USA). Each print was performed using the following print parameters: 0.4 mm nozzle diameter, 0.2 mm layer height, 100% concentric infill, YZ print orientation.

In addition to the 3D-printed test specimens, a cut-to-size Carbon Ankle Seven made of carbon composite and a manually fabricated carbon prepreg strut were idealized and measured. All specimen variants are shown in Fig. 5. In terms of the posterior struts, it was possible to clamp them at different distances from the VAJC resulting in three clamping positions with distances of +75 mm, 0 mm, and -75 mm between the bending edge of the clamp and the VAJC.

In total, ten idealized orthosis variants with clinically relevant geometries were derived; their geometric relationships are summarized in Table 2 and shown in Fig. 5 and Fig. 6.

II.VI. Test procedure

Following printing, the cross-sectional area of each specimen was measured at three points using a caliper, averaged, and used to calculate the area moment of inertia. The flexural moduli for all materials were determined via three-point bending tests (ISO 178:2019 [37]) using a universal testing machine with an extensometer (AllroundLine, ZwickRoell, Ulm, Germany). For the specimens made of carbon fiber reinforced Onyx, the CA7, and the manually fabricated posterior strut, the flexural modulus was determined using a three-point bending test on the test specimens themselves, as it was not feasible to manufacture ISO-conform three-point bending samples made of these materials. With these properties known, the

stiffness of each idealized orthosis was measured on the test bench. For this purpose, the idealized cuffs were manufactured from aluminum and specimens were cyclically deflected $\pm 5^\circ$ at 1.66°/s. A micrometer dial gauge (Käfer Messuhrenfabrik GmbH & Co. KG, Villingen-Schwenningen, Germany) positioned perpendicular to the foot cuff near the bending edge monitored potential setup deformations. Each measurement comprised five deflection cycles and was repeated three times per material and configuration. The stiffness values were then derived using linear regression over all deflection cycles and the whole range of motion. The three measured stiffness values per configuration and material were then averaged resulting in the average measured stiffness $k_{AFO, meas}$. Concurrently, theoretical stiffness $k_{AFO, calc}$ was calculated using the developed analytical method.

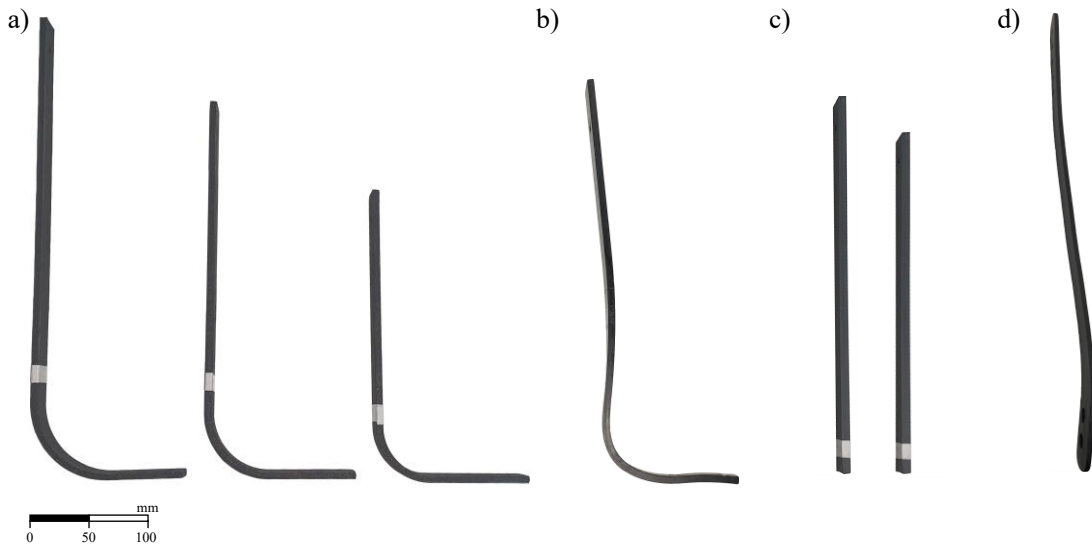


Figure 5: Tested functional elements, a) Posterior Leaf Springs (3D-Printed), b) Carbon Ankle Seven (carbon composite), c) Posterior Struts (3D-Printed), d) Carbon Prepreg Strut (carbon prepreg).

Table 2: Geometric relationships of the idealized orthoses, LS = Leaf Spring (3D-printed), CA7 = Carbon Ankle Seven (carbon composite), PS = Posterior Strut (3D-printed), CPS = Carbon Posterior Strut (prepreg).

Configuration		Posterior Leaf Spring				Posterior Strut					
		LS1	LS2	LS3	CA7	+75 mm		0 mm		-75 mm	
						PS1	PS2	PS3	CPS1	PS4	CPS2
l_{FAP}	[mm]	130.5	205.5	280.5	220.5	265	330	255	288	180	213
l_{EP}	[mm]	105.5	180.5	255.5	185.5	240	305	230	258	155	183
l_B	[mm]	175	240	305	261	190	255	255	288	255	288
l_D	[mm]	150	215	280	226	165	230	230	258	230	258
R	[mm]	40	50	60	41	0	0	0	0	0	0

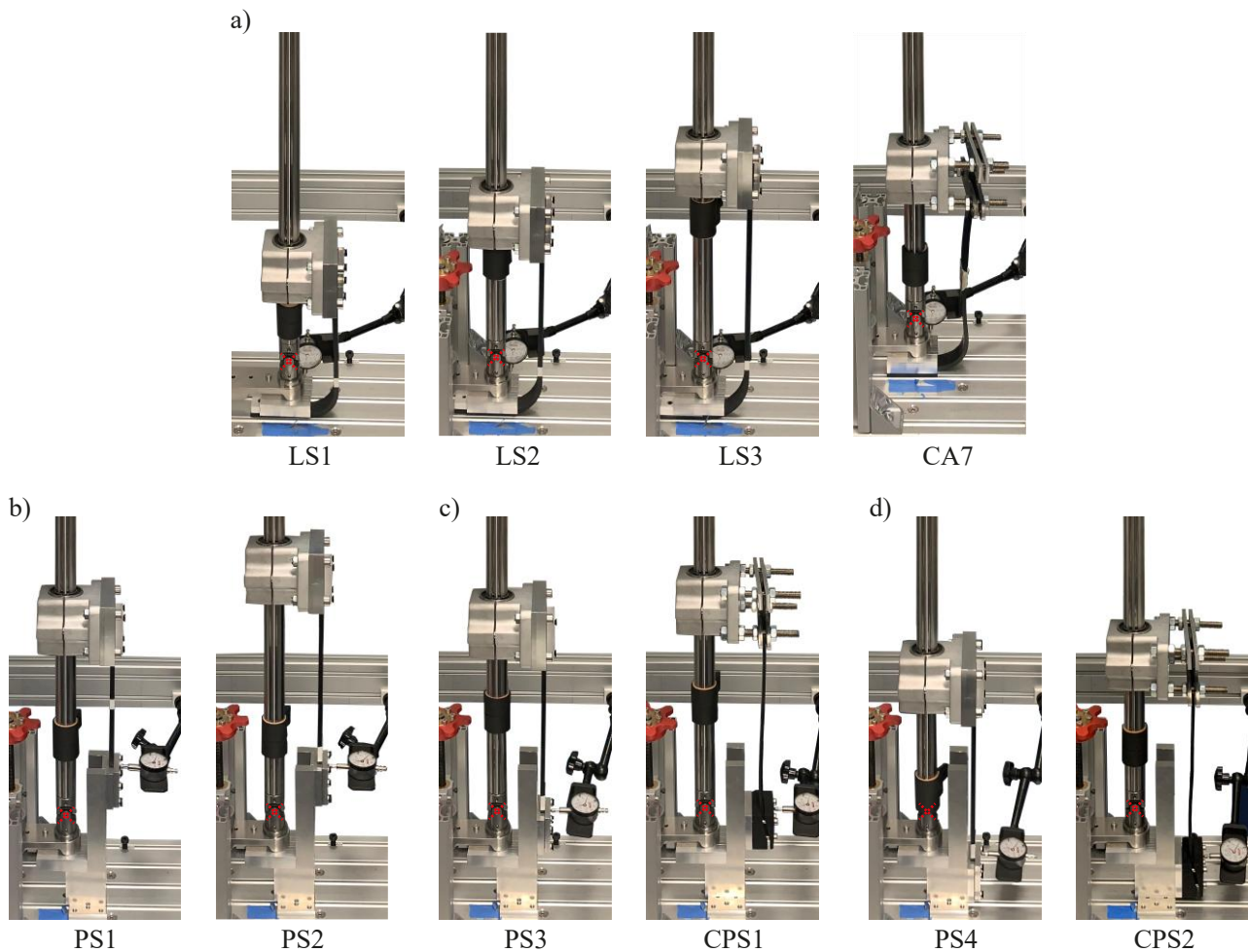


Figure 6: Idealized orthoses, a) posterior leaf springs, b) posterior struts – “+75 mm” clamping position, c) posterior struts – “0 mm” clamping position, d) posterior struts – “-75 mm” clamping position, red cross = position of VAJC.

III. Results and discussion

The calculation and measurement results are compared below and shown in Table 3, Table 5 and Fig. 8. Due to the extensive amount of data, only the mean values are presented.

III.I Leaf springs

The leaf springs results can be found in Table 3. No abnormalities or deformations of the test setup were observed during the measurement.

As can be seen, the calculated stiffness values $k_{AFO,calc}$ agree well with the physically measured stiffness values $k_{AFO,meas}$. On average, the deviation is less than 5%. The maximum deviation occurs in configuration LS1 with the material PPACF and amounts to 10%. Given the assumptions and simplifications, these deviations can be considered sufficiently small to validate the calculation method. Also, calculations for the CA7, which is used in everyday clinical practice, yield promising results with a deviation of 1%, even though its actual geometry was only approximated in the calculations. This demonstrates that the calculation method for functional elements in the form of a posterior leaf spring produces accurate predictions.

III.II Posterior struts

Unlike with the posterior leaf springs, the micrometer gauge showed deformations of the test bench/setup during measurement of the posterior struts in the clamping positions “+75 mm” and “0 mm,” which violates assumption A2 required for the calculation. For the clamping position “-75 mm” the micrometer gauge showed no deflection. Similarly, the mathematical model's predictions for the clamping positions “+75 mm” and “0 mm” are significantly less accurate than those for the “-75 mm” position. The results are presented in Table 5 (“Calculation without k_{TB} ”).

The average maximum deviation for the clamping positions “+75 mm” and “0 mm” is 50%, and the total maximum deviation observed for the “PS1” configuration and the PPACF material is 60%, which is clearly too high for validating the mathematical model for posterior struts. Nevertheless, it is notable here that the predictions for the clamping position “-75 mm,” at which the micrometer gauge showed no deflection, correspond significantly better with the measured values, with an average deviation of <6%. This leads to the assumption that the deformation of the test bench/setup and the resulting violation of assumption A2 is the reason for the high deviations.

Table 3: Results of Leaf Spring measurement, SD = standard deviation.

		Measurement			Calculation		
		I [mm ⁴]	$k_{AFO,meas}$ [Nm/°]	SD [%]	$k_{AFO,calc}$ [Nm/°]	Δ abs. [Nm/°]	Δ rel. [%]
<i>Flexural Moduli:</i> PLA = 2.82 GPa; niceBIO = 4.59 GPa; GTP = 5.14 GPa; PPACF = 11.44 GPa; Onyx with CCFR = 21.89 GPa; Carbon Composite = 67.44 GPa							
LS1	PLA	498.48	0.11	0.58	0.12	0.006	5
	niceBIO	368.63	0.14	0.93	0.14	-0.003	-2
	GTP	450.53	0.18	0.91	0.19	0.010	5
	PPACF	453.79	0.39	0.90	0.43	0.038	10
	Onyx with CCFR	491.87	0.89	0.86	0.88	-0.002	0
	Mean ± SD					0.01 ± 0.01	4 ± 4
LS2	PLA	499.21	0.10	1.02	0.10	0.001	1
	niceBIO	372.06	0.12	0.48	0.12	-0.003	-3
	GTP	456.53	0.16	0.62	0.17	0.001	1
	PPACF	457.16	0.35	0.30	0.37	0.025	7
	Onyx with CCFR	476.65	0.77	1.35	0.74	-0.033	-4
	Mean ± SD					-0.00 ± 0.02	1 ± 4
LS3	PLA	486.08	0.10	2.37	0.09	-0.005	-5
	niceBIO	371.65	0.12	1.85	0.12	-0.006	-5
	GTP	462.58	0.16	0.74	0.16	0.002	2
	PPACF	452.81	0.34	0.17	0.35	0.008	2
	Mean ± SD					0.00 ± 0.01	0 ± 3
CA7	Carbon Composite	383.35	1.94	0.47	1.96	0.019	1
	Mean ± SD					0.02 ± 0.00	1 ± 0

Mathematically accounting for these deformations would require a detailed characterization and mathematical modeling of all test bench components. However, given the existing simplifications, this is not feasible within the scope of a pen and paper calculation. For this reason, a more practical approach was chosen, which allows the deformation of the test bench to be considered in the mathematical model. Therefore, the test bench deformation behavior was approximated by modifying the mechanical model using simple theoretical tools: the ideal clamping assumption for posterior struts at the foot cuff was replaced by modelling a coupling of the struts to a torsion spring with stiffness k_{TB} , representing the equivalent torsional stiffness of the test bench. The adjusted mechanical equivalent model is shown in Fig. 7. Regarding the calculation, the coefficients expand to those in Table 4.

The torsion spring stiffness k_{TB} is assumed independent of the test specimens and constant within each clamping position but varies between the clamping positions due to differences in height and lever arm ratios. This results in distinct torsion spring stiffness values for each clamping position. To determine this clamping-position-specific stiffness value of the torsion spring $k_{TB,i}$, it must be derived

from a calibration measurement within this clamping position. After determination, it can then be applied to all subsequent stiffness calculations for that position. It should be noted that this transforms the previously purely predictive model into a calibrated model that requires actual measured input values.

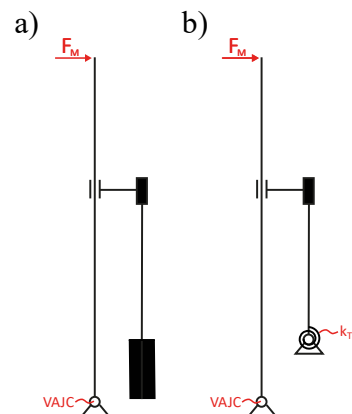


Figure 7: Adjusted mechanical equivalent model with a torsion spring to model the test bench's inherent stiffness, a) Original model, b) Adjusted model with torsion spring at the foot cuff.

Table 4: Adapted coefficients considering k_{TB} .

A	$R^2 + \frac{\pi}{2} R \cdot l_B + l_B \cdot l_D - \frac{1}{2} l_D^2 + \frac{l_B \cdot E \cdot I}{k_{TB}}$
B	$\frac{\pi}{2} R + l_D + \frac{E \cdot I}{k_{TB}}$
C	$\frac{\pi}{4} R^3 + (l_B + l_D) \cdot R^2 + \frac{\pi}{2} \cdot R \cdot l_B \cdot l_D + \frac{1}{2} \cdot l_B \cdot l_D^2 - \frac{1}{6} \cdot l_D^3 + \frac{l_B \cdot l_D \cdot E \cdot I}{k_{TB}}$
D	$R^2 + \frac{\pi}{2} R \cdot l_D + \frac{1}{2} \cdot l_D^2 + \frac{l_D \cdot E \cdot I}{k_{TB}}$

Since there was no option to carry out calibration measurements on independent test samples during the study, the specific torsional spring stiffnesses $k_{TB,+75}$ and $k_{TB,0}$ were determined based on measurements of the PLA struts in the “PS2” and “PS3” configurations, respectively. That way, the determined specific torsional spring stiffnesses were as 2.79 Nm/° for the “+75 mm” clamping position and 4.36 Nm/° for clamping position “0 mm”. Since no test bench deformation was observed at the “-75 mm” position, an ideally rigid torsion spring was assumed there, implying an infinite $k_{TB,-75}$. Incorporating these $k_{TB,i}$ -values into the adjusted model yields results presented in Table 5 (“Calculation with k_{TB} ”).

Table 5: Results of Posterior Strut measurement, SD = standard deviation.

Flexural Moduli: PLA = 2.71 GPa; niceBIO = 5.22 GPa; GTP = 5.35 GPa; PPACF = 11.43 GPa; Carbon Prepreg = 31.11 GPa												
		I [mm ⁴]	Measurement		Calculation (without k_{TB})			Calculation (with k_{TB})				
			$k_{AFO,meas}$ [Nm/°]	SD [%]	$k_{AFO,calc}$ [Nm/°]	Δ abs. [Nm/°]	Δ rel. [%]	$k_{AFO,calc}$ [Nm/°]	Δ abs. [Nm/°]	Δ rel. [%]		
+75 mm ($k_{TB,+75} = 2.792$ Nm/°)	PS1	PLA	499.21	1.28	1.27	1.71	0.429	34	1.43	0.155	12	
		niceBIO	372.06	1.56	2.35	2.45	0.887	57	1.92	0.359	23	
		GTP	456.53	2.06	1.28	3.08	1.023	50	2.29	0.237	12	
		PPACF	457.16	4.11	0.67	6.59	2.482	60	3.83	-0.278	-7	
		Mean ± SD					1.21 ± 0.69	50 ± 9		0.12 ± 0.21	10 ± 10	
	PS2	PLA	486.14	0.80	1.95	0.92	0.117	15	Calibration Sample			
		niceBIO	371.65	1.05	0.27	1.35	0.308	29	1.13	0.082	8	
		GTP	462.58	1.34	0.74	1.73	0.387	29	1.37	0.032	2	
		PPACF	452.81	2.69	0.44	3.61	0.915	34	2.36	-0.335	-12	
		Mean ± SD					0.43 ± 0.26	27 ± 7		-0.07 ± 0.16	-1 ± 7	
0 mm ($k_{TB,0} = 4.363$ Nm/°)	PS3	PLA	486.08	0.37	1.26	0.40	0.033	9	Calibration Sample			
		niceBIO	371.65	0.47	0.38	0.59	0.120	26	0.52	0.050	11	
		GTP	462.58	0.62	0.57	0.75	0.134	22	0.65	0.029	5	
		PPACF	452.81	1.28	0.44	1.57	0.296	23	1.16	-0.121	-9	
		Mean ± SD					0.15 ± 0.09	20 ± 6		-0.01 ± 0.07	2 ± 7	
	CPS1	Carbon Prepreg	196.14	1.39	2.37	1.65	0.257	18	1.20	-0.193	-14	
		Mean ± SD					0.26 ± 0.00	18 ± 0		-0.19 ± 0.00	-14 ± 0	
	-75 mm ($k_{TB,-75} = \infty$ Nm/°)	PS4	PLA	486.08	0.15	0.68	0.14	-0.008	-6	0.14	-0.008	-6
			niceBIO	371.65	0.19	1.83	0.20	0.009	4	0.20	0.009	4
			GTP	462.58	0.25	0.67	0.26	0.004	2	0.26	0.004	2
PPACF			452.81	0.52	0.30	0.54	0.015	3	0.54	0.015	3	
Mean ± SD							0.01 ± 0.01	1 ± 3		0.01 ± 0.01	1 ± 3	
CPS2		Carbon Prepreg	196.14	0.60	0.47	0.63	0.033	6	0.63	0.033	6	
		Mean ± SD					0.03 ± 0.00	6 ± 0		0.03 ± 0.00	6 ± 0	

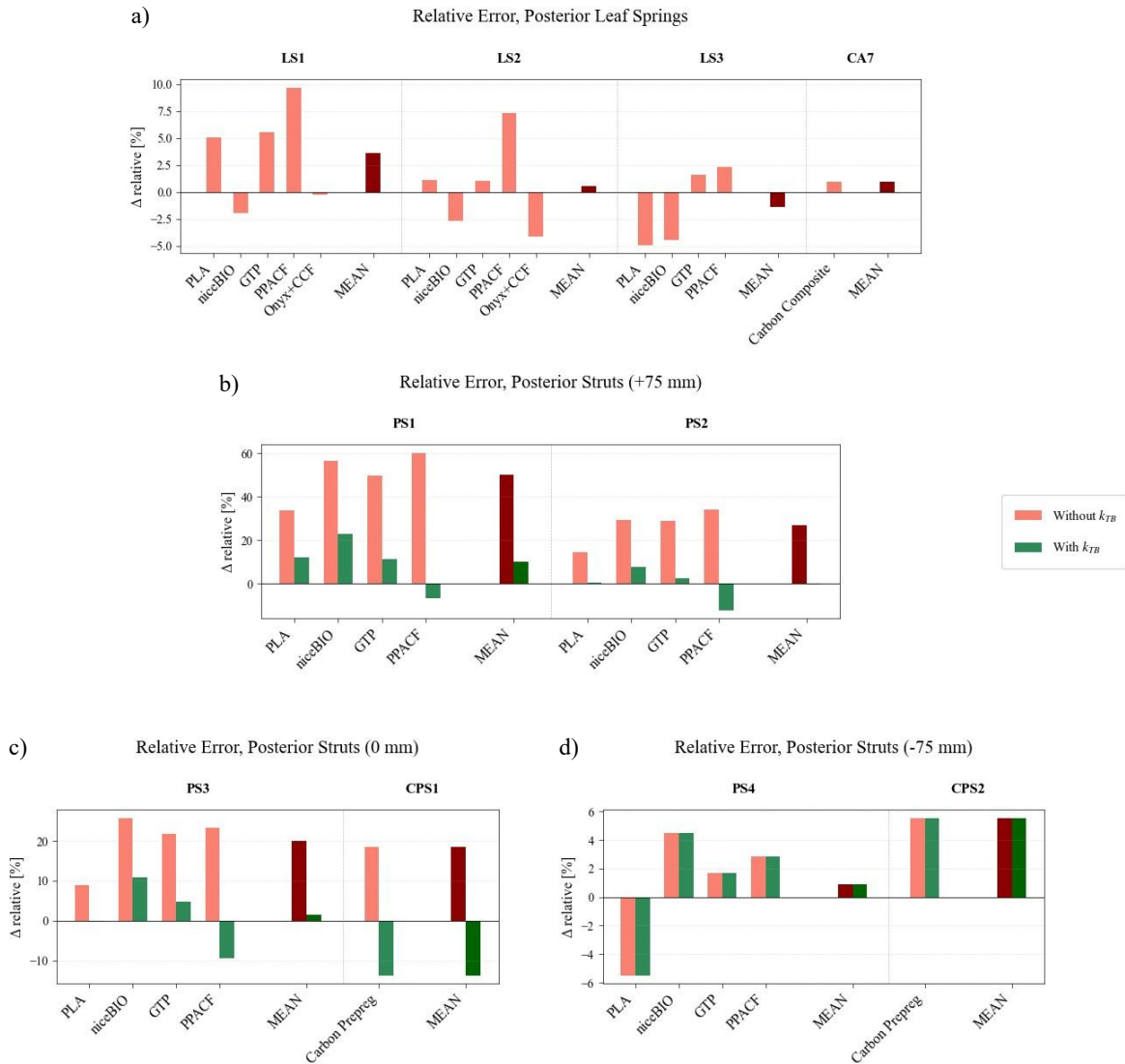


Figure 8: Relative deviation of prediction from measurement, a) posterior leaf springs, b) posterior struts – “+75 mm” clamping position, c) posterior struts – “0 mm” clamping position, d) posterior struts – “-75 mm” clamping position.

As can be seen, deviations between measured and calculated stiffnesses are significantly reduced due to the adjustment of the model: the maximum relative error at “+75 mm” drops from 60% to 23%, and at “0 mm” from 26% to 11%. Except for one outlier (PS1, niceBIO), the calibrated model can be used to predict the stiffness of all posterior struts with a maximum relative deviation of 15%, which can be considered acceptable under the assumptions, idealizations, and modeling used. This even applies to the handcrafted posterior strut used in everyday clinical practice. The effect of the model adjustment can be clearly seen in Fig. 8b & Fig. 8c.

III.III Flexural moduli and sensitivity analysis

In addition to validating the calculation methodology, the study also revealed significant discrepancies in the flexural moduli measured for the printed materials. These included significant deviations from the manufacturers’ specifications and variations between the test specimen batches printed with the leaf springs and the struts. Table 6 shows these deviations.

Although the deviations may initially appear large, it should be noted that the TDS of PLA as well as the TDS of GTP provides no specific information on the flexural, but only for the tensile modulus.

Table 6: Comparison of the mechanical properties of the printed materials.

Material	E_{TDS} [GPa]	$\frac{E_{LS}}{E_{TDS}}$ [%]	$\frac{E_{PS}}{E_{TDS}}$ [%]	$\frac{E_{PS}}{E_{LS}}$ [%]
PLA	3.5*	80.57	77.42	96.09
niceBIO	5.1**	90.00	102.35	113.72
GTP	4.3*	119.53	124.18	104.08
PPACF	9.7	117.93	117.83	99.91

*Only tensile modulus can be found in TDS
 **TDS states “flexural modulus” but references ISO 527 [38]

Although the niceBIO TDS specifies a flexural modulus, it also refers to ISO 527, which is used to determine the tensile properties of plastics [38]. It is well known that the tensile modulus and the flexural modulus for FDM-printed specimens are not the same and may vary depending on the material [39–42]. Furthermore, the TDS do not specify either the print orientation or the infill pattern of the test specimens, which further explains the deviations. Nevertheless, discrepancies also occur between the manufacturer's specifications for PPACF and the actual measured flexural moduli. Although the PPACF TDS explicitly specifies a flexural modulus and states the same printing parameters as the ones used in this study, the measured flexural moduli here are 17.9% higher.

There are also discrepancies between the test specimen batches printed together with the leaf springs and those printed together with the posterior struts. While the deviations for PLA, GTP, and PPACF are relatively small, the significant deviation of 13.7% in the niceBIO samples stands out.

The reasons for these deviations can be manifold and can be partly explained by the inherent variability of the 3D-printing process. However, these deviations may also be partly attributable to measurement errors during data collection. Such measurement errors have a direct impact on the predictions of the mathematical model. In addition to the influence of the flexural modulus, fluctuations in cross-sectional areas, as well as deviations between the geometric relationships assumed in the model and the actual geometric relationships, also influence predictions. To assess the extent to which such deviations influence the model's output, a first-order sensitivity analysis was performed for the predictive model. For this purpose, the normalized local sensitivity indices S_i of the individual input parameters were determined. In addition, a sample

calculation was performed to determine the extent to which a 5% deviation in one input variable affects the model's output. Since both values depend on the configuration-specific geometric properties, they were determined for each of the configurations described here. The results are presented in Table 7 and show the maximum and minimum values of all configurations.

As can be seen, the thickness of the functional element h has the greatest influence on the measurement result, with a normalized sensitivity index S_h of 3. It is factored into the calculation on a cubic basis. Thus, a measurement error of $\pm 5\%$ in thickness results in a deviation of $\pm 15\%$ in the calculated stiffness. The flexural modulus, on the other hand, is factored in linearly. A deviation of $\pm 13.7\%$, as observed between test specimen batches, thus results in a deviation of the same magnitude with respect to stiffness. In addition to the configuration independent influences of E , b , and h , the influence of a measurement error in the geometric parameters is configuration dependent. For example, a deviation in l_D in the "PS1" configuration has a significantly greater influence on the model's output than in the "LS1" configuration (variation of S_{l_D} from -0.71 to -2.83). Also, it can be seen that a deviation in the input parameters l_B , l_D and R has an inverse effect on the model's output, as indicated by their negative normalized sensitivity indices. For example, a deviation of $+5\%$ in l_D leads to a deviation in the calculated stiffness ranging from -3.77% to -12.92% , depending on the configuration.

The results of the sensitivity analysis thus demonstrate that the observed discrepancies between calculated and measured stiffness values are also attributable to measurement and manufacturing inaccuracies in the input variables and not necessarily to weaknesses in the model itself.

Table 7: First-order sensitivity analysis of the mathematical model for determination of $k_{AFO,calc}$

Input-parameter	S_i (min to max)	Relative change in $k_{AFO,calc}$ at $\pm 5\%$ change in the input- parameter [%]	Dependency
E	1	± 5	Linear
b^*	1	± 5	Linear
h^{**}	3	± 15	Cubic
l_{FAP}	0.03 to 1.67	± 0.56 to ± 8.37	Configuration dependent
l_{EP}	0.03 to 1.50	± 0.13 to ± 7.50	Configuration dependent
l_B	-0.04 to -1.84	± 0.21 to ± 9.19	Configuration dependent
l_D	-0.71 to -2.83	± 3.77 to ± 12.92	Configuration dependent
R	0.00 to -0.76	0.00 to ± 3.69	Configuration dependent

*Cross-section width
**Cross-section thickness

III.IV Summary

In summary, the presented calculation procedure enables sufficiently accurate stiffness prediction for idealized orthoses. If the test bench deforms, the model can be easily adjusted by calibration and still achieves good results. This holds true regardless of specimen geometry, printing material, or flexural modulus, provided the test bench's inherent stiffness is measured and applied consistently across tests. Moreover, the stiffness of two clinically used functional elements was predicted with sufficient accuracy despite significant geometric abstraction. Thus, the method offers a practical way to estimate PD-AFOs' stiffness on a test bench without complex simulations. For orthoses approximating the idealized geometries reported in this study, equation (13) can be applied directly. For other geometries, the approach can be adapted analogously, allowing stiffness predictions of different shaped functional elements or of elements with a variable cross-section if their area moment of inertia can be mathematically parameterized.

Given the critical role of orthosis stiffness in patient care, this method complements conventional post-manufacture bench testing by enabling stiffness estimation prior to fabrication. This is particularly relevant in clinical settings where iterative fitting cycles are costly and time-consuming. The method offers the opportunity to compare geometry or material variants and select a configuration meeting the patient-specific stiffness target before committing to manufacturing. This benefit is especially pronounced for additive manufacturing workflows, where geometry is freely adaptable and quickly customizable for patient-specific needs.

Furthermore, this calculation method could form the basis for extended models better tailored to clinical conditions. Future work might include adaptations for more complex geometries or factors such as orthosis cuff deformation, enhancing predictive accuracy and further optimizing PD-AFO selection and design in clinical practice.

IV. Limitations

The calculation method developed in this study relies on several assumptions and simplifications that limit the scope of the results. A central idealization is the assumption of ideally rigid orthosis cuffs (A2), which does not fully reflect reality as real cuffs deform and influence overall system stiffness. The limitation concerns the transferability of the predicted stiffness values to real-world clinical conditions. The analytical method – and the experimental validation – are both based on an idealized system with rigid cuffs, simplified geometry, and controlled boundary conditions. In clinical practice, however, AFO stiffness is influenced by additional factors not captured in this model, including cuff deformation, soft tissue interaction at the patient-orthosis interface, footwear, and individual patient anatomy [6]. As a result, the stiffness predicted by the

proposed method reflects the behavior of idealized AFOs and may differ from the stiffness of real AFOs.

Similarly, the assumption of a constant cross-sectional area (A1) restricts the method's validation to orthosis designs with approximately uniform cross-sections, such as the standardized posterior leaf springs and struts investigated in this study. In clinical practice, however, AFO geometry is considerably more complex: trimlines, varying wall thicknesses, and tapered or flared cross-sections are commonly used to fine-tune stiffness and fit individual patient needs. These geometric features directly influence the area moment of inertia along the functional element and therefore affect overall orthosis stiffness. Application and validation of the method to functional elements with variable cross-sections – for example through piecewise parameterization of the area moment of inertia – represents a promising direction for future work.

The use of Euler-Bernoulli beam theory further simplifies the model by neglecting shear deformations, which can cause deviations in specimens with high thickness-to-length ratios or small radii of curvature. Additionally, the small-angle approximation restricts the model's predictive power to deformation angles within $\pm 5^\circ$, leaving higher ranges unaddressed.

Limitations also exist regarding the model adaptation for posterior struts. While integrating an equivalent torsional spring stiffness k_{TB} significantly reduced deviations, this remains a highly simplified representation of test bench deformation. A more precise description would require detailed modeling of the entire test bench structure.

Finally, measurement equipment introduces potential error propagation. However, this was minimized through multiple measurements and averaging, as evidenced by the low standard deviations in the results (Table 3 and Table 5).

V. Conclusion

This work presents the derivation and evaluation of a simplified calculation method to determine the stiffness of idealized PD-AFOs on a test bench. Based on elastostatics and Castigliano's energy methods, and incorporating assumptions and idealizations, the method enables designers to estimate PD-AFO stiffness during the design phase without complex simulations.

Results show that calculated stiffness values for orthoses with posterior leaf springs deviate less than 10% from measured values, validating the method for these designs. For orthoses with posterior struts, stiffness predictions showed deviations of no more than 15% when using an adjusted calculation model calibrated with the test bench, which is assumed sufficiently accurate given the assumptions.

The method offers a promising alternative to finite element analysis, supporting orthosis design by enabling mathematical comparison of geometries and materials before manufacturing, especially against the background of the growing adoption of additive manufacturing in orthotic care. This enables a more efficient development process, which can lead to improved patient care in the long term.

Looking ahead, integrating additional biomechanical factors and addressing more complex geometries could expand and refine the method, enhancing its clinical applicability and may thereby improve orthopedic care quality over the long term.

ACKNOWLEDGMENTS

Research funding: Supported by the Open Access Publication Fund of FH Münster University of Applied Sciences.

AUTHOR'S STATEMENT

Conflict of interest: The authors state no conflict of interest. Animal models: No in-vivo experiments were involved with this work. Informed consent: No human participants were involved with this work. Ethical approval: No human/in-vivo participants were involved with this work.

REFERENCES

- [1] C. Zhou, Z. Yang, K. Li, X. Ye, Research and Development of Ankle-Foot Orthoses: A Review, *Sensors (Basel, Switzerland)* 22 (2022); doi: 10.3390/s22176596.
- [2] A. Aboutorabi, M. Arazpour, M. Ahmadi Bani, H. Saedi, J. S. Head, Efficacy of ankle foot orthoses types on walking in children with cerebral palsy: A systematic review, *Annals of physical and rehabilitation medicine* 60, 393–402 (2017); doi: 10.1016/j.rehab.2017.05.004.
- [3] Y. J. Choo, M. C. Chang, Commonly Used Types and Recent Development of Ankle-Foot Orthosis: A Narrative Review, *Healthcare (Basel, Switzerland)* 9 (2021); doi: 10.3390/healthcare9081046.
- [4] D. Totah, M. Menon, C. Jones-Hershinow, K. Barton, D. H. Gates, The impact of ankle-foot orthosis stiffness on gait: A systematic literature review, *Gait & posture* 69, 101–111 (2019); doi: 10.1016/j.gaitpost.2019.01.020.
- [5] T. Kobayashi, A. K. L. Leung, S. W. Hutchins, Techniques to measure rigidity of ankle-foot orthosis: a review, *Journal of rehabilitation research and development* 48, 565–576 (2011); doi: 10.1682/JRRD.2010.10.0193.
- [6] J. Z. Wang, E. A. Wojciechowski, B. Shuman, J. Burns, T. L. Cheng, Mechanical testing methods for determining stiffness of ankle-foot orthoses: A scoping review, *Prosthetics and orthotics international* (2025); doi: 10.1097/PXR.0000000000000478.
- [7] A. Wach, L. McGrady, M. Wang, B. Silver-Thorn, Assessment of Mechanical Characteristics of Ankle-Foot Orthoses, *Journal of biomechanical engineering* 140 (2018); doi: 10.1115/1.4039816.
- [8] A. Bartonek, M. Eriksson, E. M. Gutierrez-Farewik, A new carbon fibre spring orthosis for children with plantarflexor weakness, *Gait & posture* 25, 652–656 (2007); doi: 10.1016/j.gaitpost.2006.07.013.
- [9] E. Tavernese, M. Petrarca, G. Rosellini, E. Di Stanislao, A. Pisano, G. Di Rosa, E. Castelli, Carbon Modular Orthosis (Ca.M.O.): An innovative hybrid modular ankle-foot orthosis to tune the variable rehabilitation needs in hemiplegic cerebral palsy, *Neuro Rehabilitation* 40, 447–457 (2017); doi: 10.3233/NRE-161432.
- [10] B. W. Hoyt, S. Y. Nelson, J. G. Fay, S. M. Wade, D. I. Brooks, B. K. Potter, IDEO energy-storing orthosis: Effects on lower extremity function and preservation, *Injury* 52, 3505–3510 (2021); doi: 10.1016/j.injury.2021.07.023.
- [11] T. N. Pollen, A. Jor, F. Munim, Y. He, A. Daryabor, F. Gao, W.-K. Lam, T. Kobayashi, Effects of 3D-printed ankle-foot orthoses on gait: a systematic review, *Assistive technology : the official journal of RESNA* 37, 287–303 (2025); doi: 10.1080/10400435.2024.2411563.
- [12] V. Creylman, L. Muraru, J. Pallari, H. Vertommen, L. Peeraer, Gait assessment during the initial fitting of customized selective laser sintering ankle foot orthoses in subjects with drop foot, *Prosthetics and orthotics international* 37, 132–138 (2013); doi: 10.1177/0309364612451269.
- [13] E. C. Ranz, E. Russell Esposito, J. M. Wilken, R. R. Neptune, The influence of passive-dynamic ankle-foot orthosis bending axis location on gait performance in individuals with lower-limb impairments, *Clinical biomechanics (Bristol, Avon)* 37, 13–21 (2016); doi: 10.1016/j.clinbiomech.2016.05.001.
- [14] N. G. Harper, E. R. Esposito, J. M. Wilken, R. R. Neptune, The influence of ankle-foot orthosis stiffness on walking performance in individuals with lower-limb impairments, *Clinical biomechanics (Bristol, Avon)* 29, 877–884 (2014); doi: 10.1016/j.clinbiomech.2014.07.005.
- [15] E. A. Wojciechowski, T. L. Cheng, S. M. Hogan, A. J. Mudge, D. Balassone, M. P. Menezes, D. G. Little, L. N. Dwan, J. Burns, Replicating and redesigning ankle-foot orthoses with 3D printing for children with Charcot-Marie-Tooth disease, *Gait & posture* 96, 73–80 (2022); doi: 10.1016/j.gaitpost.2022.05.006.
- [16] D. J. J. Bregman, M. M. van der Krogt, V. de Groot, J. Harlaar, M. Wisse, S. H. Collins, The effect of ankle foot orthosis stiffness on the energy cost of walking: a simulation study, *Clinical biomechanics (Bristol, Avon)* 26, 955–961 (2011); doi: 10.1016/j.clinbiomech.2011.05.007.
- [17] N. F. J. Waterval, M. M. van der Krogt, K. Veerkamp, T. Geijtenbeek, J. Harlaar, F. Nollet, M. A. Brehm, The interaction between muscle pathophysiology, body mass, walking speed and ankle foot orthosis stiffness on walking energy cost: a predictive simulation study, *Journal of neuroengineering and rehabilitation* 20, 117 (2023); doi: 10.1186/s12984-023-01239-z.
- [18] A.-K. Carl, M. Kirillov, D. Hochmann, E. Quadrat, Towards credible computational models: Application of a risk based framework for establishing credibility (2023); doi: 10.18416/AMMM.2023.2309804.
- [19] C. Peng, P. Tran, S. Lalor, O. Tirosh, E. Rutz, Tuning the mechanical responses of 3D-printed ankle-foot orthoses: A numerical study, *International Journal of Bioprinting*, 3390 (2024); doi: 10.36922/ijb.3390.
- [20] J. A. Ramsey, Development of a method for fabricating polypropylene non-articulated dorsiflexion assist ankle foot orthoses with predetermined stiffness, *Prosthetics and orthotics international* 35, 54–69 (2011); doi: 10.1177/0309364610394477.
- [21] S. Behroofoot, P. E. Chatzistergos, N. Eddison, N. Chockalingam, Optimising rigid ankle foot orthoses design: A quantitative evaluation of trimlines on stiffness, *Foot (Edinburgh, Scotland)* 62, 102158 (2025); doi: 10.1016/j.foot.2025.102158.
- [22] P. E. Chatzistergos, N. Eddison, E. Ganniari-Papageorgiou, N. Chockalingam, A quantitative analysis of optimum design for rigid ankle foot orthoses: The effect of thickness and reinforcement design on stiffness, *Prosthetics and orthotics international* 48, 204–212 (2024); doi: 10.1097/PXR.0000000000000247.
- [23] A. P. Putra, A. S. Hidayat, A. Rahmatillah, Pujjiyanto, K. Ain, I. P. A. Pawana, A. W. R. Gusti, Influence of Retromalleolar Trimline Dimensions on Posterior Leaf Spring Ankle-Foot Orthosis Stiffness: A Finite Element Analysis Approach, *Mathematical Modelling of Engineering Problems* 10, 979–984 (2023); doi: 10.18280/mmep.100331.
- [24] S. Syngellakis, M. A. Arnold, H. Rassoulian, Assessment of the non-linear behaviour of plastic ankle foot orthoses by the finite element method, *Proceedings of the Institution of Mechanical Engineers. Part H, Journal of engineering in medicine* 214, 527–539 (2000); doi: 10.1243/0954411001535561.
- [25] D. Zou, T. He, M. Dailey, K. E. Smith, M. J. Silva, D. R. Sinacore, M. J. Mueller, M. K. Hastings, Experimental and computational analysis of composite ankle-foot orthosis, *Journal of rehabilitation research and development* 51, 1525–1536 (2014); doi: 10.1682/JRRD.2014.02.0046.
- [26] E. S. Schrank, L. Hitch, K. Wallace, R. Moore, S. J. Stanhope, Assessment of a virtual functional prototyping process for the rapid manufacture of passive-dynamic ankle-foot orthoses, *Journal of biomechanical engineering* 135, 101011–101017 (2013); doi: 10.1115/1.4024825.
- [27] C.-H. Yeh, K.-R. Lin, F.-C. Su, H.-Y. Hsu, L.-C. Kuo, C.-C. Lin, Optimizing 3D printed ankle-foot orthoses for patients with stroke: Importance of effective elastic modulus and finite element simulation, *Heliyon* 10, e26926 (2024); doi: 10.1016/j.heliyon.2024.e26926.
- [28] C. Koller, D. Reisman, J. Richards, E. Arch, Understanding the effects of quantitatively prescribing passive-dynamic ankle-foot orthosis bending stiffness for individuals after stroke, *Prosthetics and orthotics international* 45, 313–321 (2021); doi: 10.1097/PXR.0000000000000012.

- [29] N. F. J. Waterval, M.-A. Brehm, J. Harlaar, F. Nollet, Individual stiffness optimization of dorsal leaf spring ankle-foot orthoses in people with calf muscle weakness is superior to standard bodyweight-based recommendations, *Journal of neuroengineering and rehabilitation* 18, 97 (2021); doi: 10.1186/s12984-021-00890-8.
- [30] N. F. J. Waterval, F. Nollet, J. Harlaar, M.-A. Brehm, Modifying ankle foot orthosis stiffness in patients with calf muscle weakness: gait responses on group and individual level, *Journal of neuroengineering and rehabilitation* 16, 120 (2019); doi: 10.1186/s12984-019-0600-2.
- [31] A. Ielapi, N. Lammens, W. van Paepegem, M. Forward, J. P. Deckers, M. Vermandel, M. de Beule, A validated computational framework to evaluate the stiffness of 3D printed ankle foot orthoses, *Computer methods in biomechanics and biomedical engineering* 22, 880–887 (2019); doi: 10.1080/10255842.2019.1601712.
- [32] M. Walbran, K. Turner, A. J. McDaid, Customized 3D printed ankle-foot orthosis with adaptable carbon fibre composite spring joint, *Cogent Engineering* 3, 1227022 (2016); doi: 10.1080/23311916.2016.1227022.
- [33] E. Russell Esposito, M. D. Ruble, A. J. Ikeda, J. M. Wilken, The effect of custom carbon ankle-foot orthosis alignment on roll-over shape and center of pressure velocity, *Prosthetics and orthotics international* 45, 147–152 (2021); doi: 10.1177/0309364620971407.
- [34] E. S. Arch, S. J. Stanhope, Passive-dynamic ankle-foot orthoses substitute for ankle strength while causing adaptive gait strategies: a feasibility study, *Annals of biomedical engineering* 43, 442–450 (2015); doi: 10.1007/s10439-014-1067-8.
- [35] M. S. Khaing, M. Samala, G. Guerra, A. Wisessint, Design and mechanical testing of an adjustable posterior leaf spring ankle-foot orthosis for patients with drop foot, *Prosthetics and orthotics international* 48, 39–45 (2024); doi: 10.1097/PXR.0000000000000278.
- [36] P. Cappa, F. Patanè, M. M. Pierro, A novel device to evaluate the stiffness of ankle-foot orthosis devices, *Journal of biomechanical engineering* 125, 913–917 (2003); doi: 10.1115/1.1634993.
- [37] DIN – Deutsches Institut für Normung e. V., Kunststoffe — Bestimmung der Biegeeigenschaften: (ISO 178:2019); Deutsche Fassung EN ISO 178:2019 83.080.01 (2019).
- [38] DIN – Deutsches Institut für Normung e. V., Kunststoffe - Bestimmung der Zugeigenschaften: Teil 1: Allgemeine Grundsätze (ISO 527-1:2019); Deutsche Fassung EN ISO 527-1:2019 83.080.01 (2019).
- [39] A. A. Al-Tamimi, A. Pandžić, E. Kadrić, Investigation and Prediction of Tensile, Flexural, and Compressive Properties of Tough PLA Material Using Definitive Screening Design, *Polymers* 15 (2023); doi: 10.3390/polym15204169.
- [40] K. I. Byberg, A. W. Gebisa, H. G. Lemu, Mechanical properties of ULTEM 9085 material processed by fused deposition modeling, *Polymer Testing* 72, 335–347 (2018); doi: 10.1016/j.polymeresting.2018.10.040#.
- [41] M.-M. Pastor-Artigues, F. Roure-Fernández, X. Ayneto-Gubert, J. Bonada-Bo, E. Pérez-Guindal, I. Buj-Corral, Elastic Asymmetry of PLA Material in FDM-Printed Parts: Considerations Concerning Experimental Characterisation for Use in Numerical Simulations, *Materials (Basel, Switzerland)* 13 (2019); doi: 10.3390/ma13010015.
- [42] S. Thumsorn, W. Prasong, T. Kurose, A. Ishigami, Y. Kobayashi, H. Ito, Rheological Behavior and Dynamic Mechanical Properties for Interpretation of Layer Adhesion in FDM 3D Printing, *Polymers* 14 (2022); doi: 10.3390/polym14132721.

Appendix

Appendix to O. Strenge and D. Hochmann, “Analytical stiffness prediction method for idealized passive dynamic ankle-foot orthoses under standardized bench test conditions”, Trans. AMMM, 2026, Vol. 8, No 1, Article ID 2755

This appendix presents the derivation of the formulas listed above, which can be used to make predictions about the stiffness of passive dynamic ankle-foot orthoses (PD-AFOs). The procedure is illustrated using the example of a PD-AFO with a posterior leaf spring. However, the calculation procedure can also be used for any other spring shape, as long as the assumptions are adjusted accordingly and small deformation angles are assumed.

The following steps are taken to derive the equations, which are then explained in individual subchapters:

- A.I. Mechanical abstraction and modeling
- A.II. Definition of assumptions
- A.III. Establishing deformation equations using Castigliano's energy theorem
- A.IV. Determination of the sought-after unknowns
- A.V. Calculation of AFO stiffness

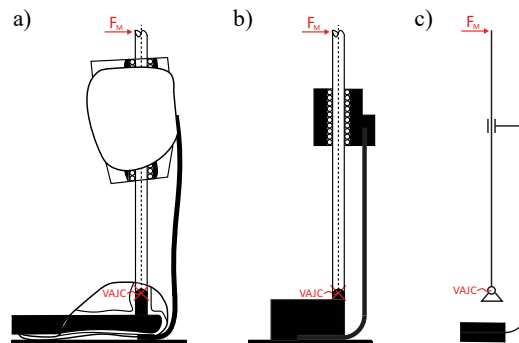
A.I. Mechanical abstraction and modeling

In reality, AFO stiffness is determined using a test bench that deforms the orthosis around a virtual ankle joint center (VAJC). As a first approximation, it can be assumed that the resistive torque generated by a PD-AFO T_{AFO} depends linearly on the deflection angle of the AFO/the deflection angle of the test bench φ . The proportionality factor is referred to as orthosis stiffness k_{AFO} and is usually specified in $Nm/^\circ$.

$$T_{AFO}(\varphi) = k_{AFO} \cdot \varphi \quad (a.1)$$

To calculate the stiffness of the orthosis on the test bench while minimizing unknown influences and being able to check the calculation results free of disturbance variables, the AFO and the test bench must first be idealized. The idealized model of test bench and orthosis can then be converted into a mechanical equivalent model (see App. Fig. 1). To do this, the following assumptions must be made:

- A1. All functional elements have a constant cross-section
- A2. The cuffs and test bench components are ideally rigid
- A3. All components are massless
- A4. The test bench's linear guide is frictionless



App. Figure 1: Idealization and modeling of the AFO, a) Real case, b) Idealized AFO, c) Mechanical replacement model

The stiffness of the system can now be calculated using the derived mechanical equivalent model.

On the test bench, the resistive moment relative to the VAJC is calculated as follows (see App. Fig. 2a):

$$T_{AFO}(\varphi) = F_M(\varphi) \cdot l_M \quad (a.2)$$

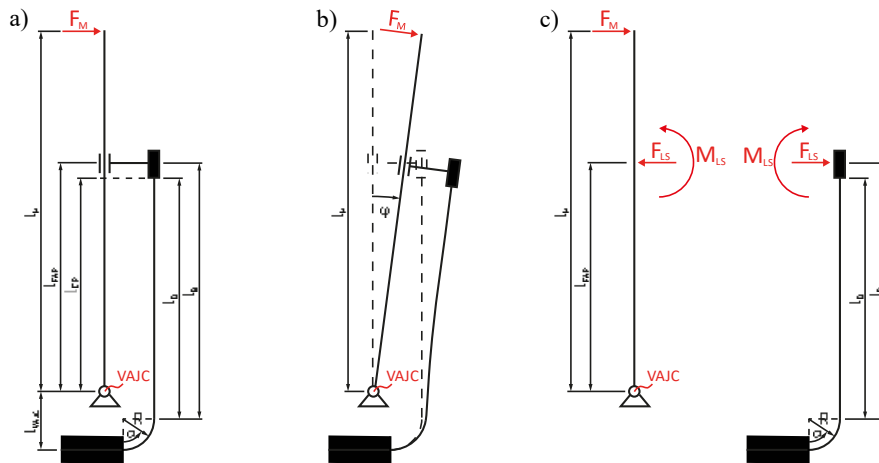
Together with equation (a.1) and the mechanical equivalent model, the stiffness relative to the VAJC can be calculated as follows (see App. Fig. 2b):

$$k_{AFO} = \frac{F_M(\varphi) \cdot l_M}{\varphi} \tag{a.3}$$

The following relationship can be derived from the geometric conditions (see App. Fig. 2a) and the free body diagram (see App. Fig. 2c):

$$k_{AFO} = \frac{T_{LS}(\varphi) + F_{LS}(\varphi) \cdot l_{FAP}}{\varphi} \tag{a.4}$$

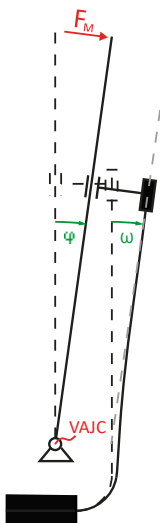
Here, $T_{LS}(\varphi)$ and $F_{LS}(\varphi)$ are the torques and forces transferred from the functional element to the test bench, respectively, and l_{FAP} is the distance between the VAJC and the point of force application (approx. at the center of the calf cuff).



App. Figure 2: Mechanical equivalent model, a) geometric relationships, b) deformation state, c) free body diagram

A.II. Definition of assumptions

To determine $T_{LS}(\varphi)$ and $F_{LS}(\varphi)$, the deformation state of the functional element must be determined as a function of the deflection angle of the test bench φ . The deformation state is characterized by the deflection f and the deformation angle ω of the AFO under the influence of force. Using the following assumptions, a relationship between f and ω with φ can be established (see App. Fig. 3 & App. Fig. 4).

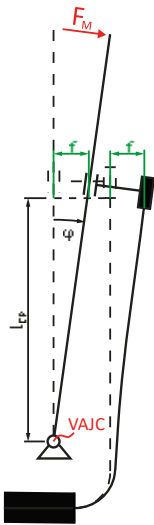


A5. The functional element's deformation angle ω at the point of its attachment to the calf cuff (at height $l_D + R$) equals the deflection angle of the test bench φ :

Assuming that the orthosis cuffs behave with ideal rigidity, the area of the functional element clamped in the calf cuff must always move parallel to the test bench. This means that the deformation angle ω of the element at the lower contact point with the calf cuff must always be equal to the deflection angle of the test bench φ . Therefore, the following applies:

$$\omega = \varphi \tag{a.5}$$

App. Figure 3: Visualization of assumption A5



A6. The functional element’s deflection f at the point of its attachment to the calf cuff (at height $l_D + R$) equals the horizontal distance traveled by the test bench at the same height.

This assumption only applies to small deformation angles of the functional element. However, since all further calculations according to the laws of elastostatics are also based on the assumption of small deformation angles, this assumption is justified.

$$f = \varphi \cdot l_{EP} \tag{a.6}$$

App. Figure 4: Visualization of assumption A6

Since ω and f depend solely on $T_{LS}(\varphi)$ and $F_{LS}(\varphi)$, the conventional formulas of bending theory can now be applied under the laws of elastostatics, thereby establishing the relationship between $T_{LS}(\varphi)$, $F_{LS}(\varphi)$ and φ .

A.III. Establishing deformation equations using Castigliano's energy theorem

Castigliano's energy theorem can be used to calculate the deformation state of a body with the given geometry. With the help of Castigliano's theorem, both the deformation angle ω and the deformation f of a body along the line of action of a force at its point of application can be calculated. To do this, the sum of the deformation energies from the individual sectional areas i of a body along its neutral axis is calculated and then converted to the desired variables. For the model shown here, the theorem can be simplified to the two deformation equations:

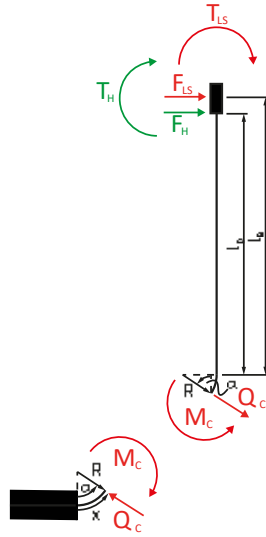
$$\omega = \sum_i \left(\int \frac{M_{C,i}}{E \cdot I} \frac{\delta M_{C,i}}{\delta T_j} dx \right) \tag{a.7}$$

$$f = \sum_i \left(\int \frac{M_{C,i}}{E \cdot I} \frac{\delta M_{C,i}}{\delta F_j} dx \right) \tag{a.8}$$

Here, $M_{C,i}$ represents the internal bending moment in the individual sections i . T_j and F_j denote the externally acting torques and forces at the point of evaluation of ω and f . E is the flexural modulus, and I is the area moment of inertia of the bending body.

The geometry of a posterior leaf spring can be divided into three sections, which can then be calculated. The evaluation point (the point where ω and f are calculated) is the lower contact point of the functional element with the calf cuff (at height $l_D + R$), as it can only deform up to this point. However, this point is not the force application point of $T_{LS}(\varphi)$ and $F_{LS}(\varphi)$ (this is located in the middle of the clamping in the calf cuff, where the force is transferred from the test bench to the leaf spring, at height $l_B + R$). However, since Castigliano's theorem can only be used to calculate the deformations at a force application point, virtual auxiliary forces (T_H and F_H) must be added at the evaluation point, which are later set to zero (see App. Fig. 5).

This results in the following free body diagram for calculating the internal forces in the functional element:



App. Figure 5: Internal forces in the functional element

For the bending moment $M_{C,i}$ along the functional element's neutral axis the following applies:

$$M_{C,1} = (\cos(\alpha(x)) \cdot R + l_D) \cdot F_H + (\cos(\alpha(x)) \cdot R + l_B) \cdot F_{LS}(\varphi) + T_H + T_{LS}(\varphi) \quad 0 < x < \frac{\pi}{2}R \quad (\text{a.9})$$

$$M_{C,2} = (l_D + \frac{\pi}{2}R - x) \cdot F_H + (l_B + \frac{\pi}{2}R - x) \cdot F_{LS}(\varphi) + T_H + T_{LS}(\varphi) \quad \frac{\pi}{2}R < x < l_D + \frac{\pi}{2}R \quad (\text{a.10})$$

$$M_{C,3} = (l_B + \frac{\pi}{2}R - x) \cdot F_{LS}(\varphi) + T_{LS}(\varphi) \quad l_D + \frac{\pi}{2}R < x < l_B + \frac{\pi}{2}R \quad (\text{a.11})$$

A.III.I. Calculation of the deflection angle ω

With the help of the bending moment, the deformation angle ω of the functional element can now be determined. Inserting the different bending moments into equation (a.7), the following results:

$$\omega = \frac{1}{E \cdot I} \left(\int_0^{\frac{\pi}{2}R} M_{C,1} \frac{\delta M_{C,1}}{\delta T_H} dx + \int_{\frac{\pi}{2}R}^{l_D + \frac{\pi}{2}R} M_{C,2} \frac{\delta M_{C,2}}{\delta T_H} dx + \int_{l_D + \frac{\pi}{2}R}^{l_B + \frac{\pi}{2}R} M_{C,3} \frac{\delta M_{C,3}}{\delta T_H} dx \right) \quad (\text{a.12})$$

To solve this equation, the partial derivatives are first formed:

$$\frac{\delta M_{C,1}}{\delta T_H} = 1 \quad (\text{a.13})$$

$$\frac{\delta M_{C,2}}{\delta T_H} = 1 \quad (\text{a.14})$$

$$\frac{\delta M_{C,3}}{\delta T_H} = 0 \quad (\text{a.15})$$

If the partial derivatives and $M_{C,i}$ for the individual sections are now inserted into equation (a.12) and $M_H = F_H = 0$ is set, the following applies:

$$\omega = \frac{1}{E \cdot I} \left(\int_0^{\frac{\pi}{2}R} ((\cos(\alpha(x)) \cdot R + l_B) \cdot F_{LS}(\varphi) + T_{LS}(\varphi)) dx + \int_{\frac{\pi}{2}R}^{l_D + \frac{\pi}{2}R} \left((l_B + \frac{\pi}{2}R - x) \cdot F_{LS}(\varphi) + T_{LS}(\varphi) \right) dx \right) \quad (\text{a.16})$$

As can be seen, two integrals must be solved.

First, the first integral is solved:

$$I_1 = \int_0^{\frac{\pi}{2}R} ((\cos(\alpha(x)) \cdot R + l_B) \cdot F_{LS}(\varphi) + T_{LS}(\varphi)) dx \quad (\text{a.17})$$

To solve this integral, a relationship between α and x must be found. The geometric relationships yield:

$$x = R \cdot \alpha \quad (\text{a.18})$$

And thus:

$$dx = R \cdot d\alpha \quad (\text{a.19})$$

With this coordinate transformation, equation (a.17) yields:

$$I_1 = \int_0^{\frac{\pi}{2}} ((\cos(\alpha) \cdot R + l_B) \cdot F_{LS}(\varphi) + T_{LS}(\varphi)) \cdot R \cdot d\alpha \quad (\text{a.20})$$

Resolved to:

$$I_1 = F_{LS}(\varphi) \cdot \left(R^2 + \frac{\pi}{2}R \cdot l_B \right) + T_{LS}(\varphi) \cdot \frac{\pi}{2}R \quad (\text{a.21})$$

Since the second integral is linearly dependent on x , no substitution is necessary in this case, and it can be integrated directly:

$$I_2 = \int_{\frac{\pi}{2}R}^{l_D + \frac{\pi}{2}R} \left((l_B + \frac{\pi}{2}R - x) \cdot F_{LS}(\varphi) + T_{LS}(\varphi) \right) dx \quad (\text{a.22})$$

Resolved to:

$$I_2 = F_{LS}(\varphi) \cdot \left(l_B \cdot l_D - \frac{1}{2}l_D^2 \right) + T_{LS}(\varphi) \cdot l_D \quad (\text{a.23})$$

Substituting the solutions of the integrals into equation (a.16) yields the following for the deformation angle ω at the evaluation point:

$$\omega = \frac{1}{E \cdot I} \left(F_{LS}(\varphi) \cdot \left(R^2 + \frac{\pi}{2}R \cdot l_B + l_B \cdot l_D - \frac{1}{2}l_D^2 \right) + T_{LS}(\varphi) \cdot \left(\frac{\pi}{2}R + l_D \right) \right) \quad (\text{a.24})$$

A.III.II. Calculation of the deformation f

Analogously, the deflection f of the functional element at the edge of the calf cuff is calculated. Equation (a.8) therefore yields:

$$f = \frac{1}{E \cdot I} \left(\int_0^{\frac{\pi}{2}R} M_{C,1} \frac{\delta M_{C,1}}{\delta F_H} dx + \int_{\frac{\pi}{2}R}^{l_D + \frac{\pi}{2}R} M_{C,2} \frac{\delta M_{C,2}}{\delta F_H} dx + \int_{l_D + \frac{\pi}{2}R}^{l_B + \frac{\pi}{2}R} M_{C,3} \frac{\delta M_{C,3}}{\delta F_H} dx \right) \quad (\text{a.25})$$

First, the partial derivatives are formed again:

$$\frac{\delta M_{C,1}}{\delta F_H} = \cos(\alpha(x)) \cdot R + l_D \quad (\text{a.26})$$

$$\frac{\delta M_{C,2}}{\delta F_H} = l_D + \frac{\pi}{2}R - x \quad (\text{a.27})$$

$$\frac{\delta M_{C,3}}{\delta F_H} = 0 \quad (\text{a.28})$$

Substituting into equation (a.25) with $T_H = F_H = 0$, the following results:

$$f = \frac{1}{E \cdot I} \left(\int_0^{\frac{\pi}{2}R} ((\cos(\alpha(x)) \cdot R + l_B) \cdot F_{LS}(\varphi) + T_{LS}(\varphi)) \cdot (\cos(\alpha) \cdot R + l_D) dx + \int_{\frac{\pi}{2}R}^{l_D + \frac{\pi}{2}R} \left((l_B + \frac{\pi}{2}R - x) \cdot F_{LS}(\varphi) + T_{LS}(\varphi) \right) \cdot \left(l_D + \frac{\pi}{2}R - x \right) dx \right) \quad (\text{a.29})$$

Here, too, there are two integrals to solve.

First, the first integral is solved again:

$$I_1 = \int_0^{\frac{\pi}{2}R} ((\cos(\alpha(x)) \cdot R + l_B) \cdot F_{LS}(\varphi) + T_{LS}(\varphi)) \cdot (\cos(\alpha) \cdot R + l_D) dx \quad (\text{a.30})$$

Similarly, a coordinate transformation is performed here, resulting in:

$$I_1 = \int_0^{\frac{\pi}{2}} ((\cos(\alpha) \cdot R + l_B) \cdot F_{LS}(\varphi) + T_{LS}(\varphi)) \cdot (\cos(\alpha) \cdot R + l_D) \cdot R \cdot d\alpha \quad (\text{a.31})$$

Which resolves to:

$$I_1 = F_{LS}(\varphi) \cdot \left(\frac{\pi}{4} R^3 + (l_B + l_D) \cdot R^2 + \frac{\pi}{2} \cdot R \cdot l_B \cdot l_D \right) + T_{LS}(\varphi) \cdot \left(R^2 + \frac{\pi}{2} R \cdot l_D \right) \quad (\text{a.32})$$

The second integral is calculated as follows:

$$I_2 = \int_{\frac{\pi}{2}R}^{l_D + \frac{\pi}{2}R} \left((l_B + \frac{\pi}{2}R - x) \cdot F_{LS}(\varphi) + T_{LS}(\varphi) \right) \cdot \left(l_D + \frac{\pi}{2}R - x \right) dx \quad (\text{a.33})$$

Which resolves to:

$$I_2 = F_{LS}(\varphi) \cdot \left(\frac{1}{2} \cdot l_B \cdot l_D^2 - \frac{1}{6} \cdot l_D^3 \right) + T_{LS}(\varphi) \cdot \left(\frac{1}{2} \cdot l_D^2 \right) \quad (\text{a.34})$$

This result for the deflection f of the functional element at the evaluation point yields:

$$f = \frac{1}{E \cdot I} \left(F_{LS}(\varphi) \cdot \left(\frac{\pi}{4} R^3 + (l_B + l_D) \cdot R^2 + \frac{\pi}{2} \cdot R \cdot l_B \cdot l_D + \frac{1}{2} \cdot l_B \cdot l_D^2 - \frac{1}{6} \cdot l_D^3 \right) + T_{LS}(\varphi) \cdot \left(R^2 + \frac{\pi}{2} R \cdot l_D + \frac{1}{2} \cdot l_D^2 \right) \right) \quad (\text{a.35})$$

A.III.III. Deformation equations

The deformation equations at the evaluation point are therefore:

$$\omega = \frac{1}{E \cdot I} \left(F_{LS}(\varphi) \cdot \left(R^2 + \frac{\pi}{2} R \cdot l_B + l_B \cdot l_D - \frac{1}{2} l_D^2 \right) + T_{LS}(\varphi) \cdot \left(\frac{\pi}{2} R + l_D \right) \right) \quad (\text{a.24})$$

$$f = \frac{1}{E \cdot I} \left(F_{LS}(\varphi) \cdot \left(\frac{\pi}{4} R^3 + (l_B + l_D) \cdot R^2 + \frac{\pi}{2} \cdot R \cdot l_B \cdot l_D + \frac{1}{2} \cdot l_B \cdot l_D^2 - \frac{1}{6} \cdot l_D^3 \right) + T_{LS}(\varphi) \cdot \left(R^2 + \frac{\pi}{2} R \cdot l_D + \frac{1}{2} \cdot l_D^2 \right) \right) \quad (\text{a.35})$$

A.IV. Determination of the sought-after unknowns

With the now known relationships between the deformation state as a function of $T_{LS}(\varphi)$ and $F_{LS}(\varphi)$, a relationship to φ can be derived using the assumptions A5 & A6. Substituting equations (a.24) and (a.35) into the equations (a.5) and (a.6) yields the following relationships:

$$\varphi = \frac{1}{E \cdot I} \left(F_{LS}(\varphi) \cdot \left(R^2 + \frac{\pi}{2} R \cdot l_B + l_B \cdot l_D - \frac{1}{2} l_D^2 \right) + T_{LS}(\varphi) \cdot \left(\frac{\pi}{2} R + l_D \right) \right) \quad (\text{a.36})$$

$$\varphi \cdot l_{EP} = \frac{1}{E \cdot I} \left(F_{LS}(\varphi) \cdot \left(\frac{\pi}{4} R^3 + (l_B + l_D) \cdot R^2 + \frac{\pi}{2} \cdot R \cdot l_B \cdot l_D + \frac{1}{2} \cdot l_B \cdot l_D^2 - \frac{1}{6} \cdot l_D^3 \right) + T_{LS}(\varphi) \cdot \left(R^2 + \frac{\pi}{2} R \cdot l_D + \frac{1}{2} \cdot l_D^2 \right) \right) \quad (\text{a.37})$$

Since both the material properties and all geometric relationships are constants, these relationships correspond to a linear system of equations that can be used to explicitly calculate $T_{LS}(\varphi)$ and $F_{LS}(\varphi)$.

The following substitutions are made to solve the linear system of equations:

$$A = R^2 + \frac{\pi}{2} R \cdot l_B + l_B \cdot l_D - \frac{1}{2} l_D^2 \quad (\text{a.38})$$

$$B = \frac{\pi}{2} R + l_D \quad (\text{a.39})$$

$$C = \frac{\pi}{4} R^3 + (l_B + l_D) \cdot R^2 + \frac{\pi}{2} \cdot R \cdot l_B \cdot l_D + \frac{1}{2} \cdot l_B \cdot l_D^2 - \frac{1}{6} \cdot l_D^3 \quad (\text{a.40})$$

$$D = R^2 + \frac{\pi}{2} R \cdot l_D + \frac{1}{2} \cdot l_D^2 \quad (\text{a.41})$$

Thus, the linear system of equations can be simplified as follows:

$$\varphi = \frac{1}{E \cdot I} (F_{LS}(\varphi) \cdot A + T_{LS}(\varphi) \cdot B) \quad (\text{a.42})$$

$$\varphi \cdot l_{EP} = \frac{1}{E \cdot I} (F_{LS}(\varphi) \cdot C + T_{LS}(\varphi) \cdot D) \quad (\text{a.43})$$

Solving for $T_{LS}(\varphi)$ and $F_{LS}(\varphi)$ yields:

$$T_{LS}(\varphi) = E \cdot I \cdot \varphi \cdot \frac{l_{EP} \cdot A - C}{D \cdot A - B \cdot C} \quad (\text{a.44})$$

$$F_{LS}(\varphi) = E \cdot I \cdot \varphi \cdot \frac{l_{EP} \cdot B - D}{C \cdot B - A \cdot D} \quad (\text{a.45})$$

A.V. Calculation of AFO stiffness

The equation for calculating the stiffness of the idealized orthosis is:

$$k_{AFO} = \frac{T_{LS}(\varphi) + F_{LS}(\varphi) \cdot l_{FAP}}{\varphi} \quad (\text{a.4})$$

Using relations (a.44) and (a.45) determined in the previous section, the following applies:

$$k_{AFO} = E \cdot I \cdot \left(\frac{l_{EP} \cdot A - C}{D \cdot A - B \cdot C} + l_{FAP} \cdot \frac{l_{EP} \cdot B - D}{C \cdot B - A \cdot D} \right) \quad (\text{a.46})$$